Rev. Roum. Sci. Techn.– Électrotechn. et Énerg.
Vol. **69**, *3*, pp. 353–358, Bucarest, 2024

SIMULATION OF BIOMASS CARBONIZATION AND HEAT RECOVERY FOR ELECTRICITY PRODUCTION USING SEEBECK MODULES

HERVÉ KLINKLIN BADAKA[1,*], ALEXANDRU M. MOREGA[2]

Keywords: Pyrolysis; Wood biomass; Seebeck effect; Finite element method (FEM); Numerical simulation.

This paper experimentally and numerically examines biomass carbonization and using thermoelectric modules to recover heat and generate electricity using the finite element method (FEM). Carbonization, conducted at high temperatures, produces charcoal and gases. The study identifies optimal temperatures for module placement, demonstrating that they can generate up to 6.5 W of electricity. Moreover, integrating the chimney to optimize the carbonization process produced hot air with a maximum gain of 11 °C above the ambient temperature. This approach enhances energy efficiency and reduces costs.

1. INTRODUCTION

The transition to more sustainable and environmentally friendly energy sources has become a global priority in the face of the challenges posed by climate change and the depletion of fossil fuel reserves [1]. In this context, the valorization of biomass emerges as a promising solution. Biomass carbonization is a complex process where heat transforms biomass into charcoal. Engineers and researchers use advanced simulation tools to optimize this process and produce more energy, *e.g.*, [2]. It accurately models heat, chemical reactions, and gas flows, helping to analyze and improve carbonization. To optimize carbonization, it's crucial to recover the heat produced.

An innovative solution uses thermoelectric (TEC) Seebeck modules, which convert heat directly into electricity using the Seebeck effect. This effect harnesses temperature differences to generate electricity, offering an efficient method of energy recovery [3].

Integrating these modules into carbonization reactors creates a more efficient and sustainable energy production system. This study models biomass carbonization and integrates TEC modules to recover heat for electricity production. We aim to improve the energy efficiency of the carbonization process and propose an innovative renewable energy solution.

We will explore the simulation steps, operational principles of Seebeck modules, and the benefits and prospects of this integrated approach. The simulations examined product yield, wood chip pyrolysis kinetics, module placement, and the electrical power generated by a module. Simulation results of autothermal pyrolysis of wood chips were compared with experimental studies.

2. MATERIAL AND METHODS

The carbonization device consists of three coaxial cylinders: an 8 cm-diameter inner chimney and intermediate and outer cylinders with 30 cm and 40 cm diameters, respectively. All cylinders are 40 cm tall. The space between the outer cylinders is filled with a clay-sawdust mixture to reduce heat loss.

Carbonization occurs in the space between the two smaller cylinders using an auto thermal method (Fig. 1), starting with partially combusting 3.5 kg of sun-dried wood chips. Temperature is monitored with a type K thermocouple during the two-hour process.

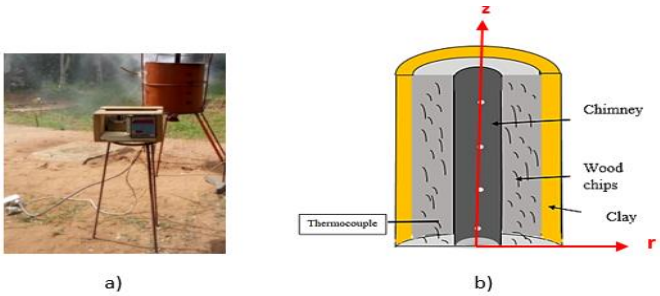

Fig. 1 – a) Photo of the experimental setup; b) Schematic cross-section of the carbonizer.

3. NUMERICAL MODELING OF CARBONIZER

A 2D model was developed, integrating heat and mass transfer with chemical reactions. The main assumptions used for the modeling are that the carbonizer (a porous reactive medium), the gas, and the solid are in local thermal equilibrium; the fluid flow in the carbonization chamber is described by Darcy flow. The chimney evaporation by laminar flow is not considered.

3.1. REACTION SCHEME AND KINETICS PARAMETERS

Carbonization decomposes organic materials at 400-1000°C in low or no oxygen, producing carbon-rich products like charcoal, tar, and pyrolysis gases [4]. This work uses the reaction scheme in Fig. 2, where wood decomposes into tar, charcoal, and gas, with some tar further decomposing into additional gas and charcoal [5].

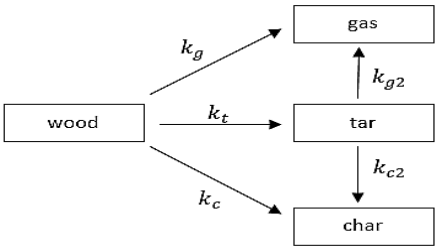

Fig. 2 – Kinetics of the model.

The Arrhenius equation provides the temperature dependence of reaction rates:

[1,*] Centre d'Excellence Régional pour la Maîtrise de l'Electricité (CERME), Université de Lomé, Togo. (Correspondence)
[2] Faculty of Electrical Engineering, National University of Science and Technology Politehnica Bucharest, Romania
E-mails: herve.badaka@gmail.com, alexandru.morega@upb.ro

DOI: 10.59277/RRST-EE.2024.69.3.17

$$k_i = A_i e^{-\frac{E_i}{RT}}, \quad (1)$$

where k_i [s^{-1}] is the rate constant of reaction, A_i [s^{-1}] is the pre-exponential factor, and E_i [J/mol] is the activation energy. The kinetic parameters and heat of the reaction are listed in Table 1. Here Δh_i [kJ/kg] is the heat of pyrolysis, c is the primary char generation reaction, *t* is tar, *g* is the primary gas generation reaction, c2 is the secondary char generation reaction, and g2 is the secondary gas generation reaction.

Table 1

Model kinetics parameters and heats of pyrolysis [5].

Reaction	A_i [s^{-1}]	E_i [J/mol]	Δh_i [kJ/kg]
c	$3.27 \cdot 10^6$	11,700	64
t	$1.08 \cdot 10^{10}$	148,000	64
g	$4.38 \cdot 10^9$	152,700	64
*c*2	$1.00 \cdot 10^5$	108,000	-42
*g*2	$4.28 \cdot 10^6$	108,000	-42

3.2. GOVERNING EQUATION OF PYROLYSIS

The wood carbonization process is a fully coupled multiphysics problem involving mass transfer, fluid flow, and heat transfer [6].

3.2.1. *Mass transport*

The equations governing the evolution of solid species, wood (*w*) and charcoal (*c*), are:

$$\frac{\partial \rho_w}{\partial t} = S_w = -(k_t + k_g + k_c)\rho_w, \quad (2)$$

$$\frac{\partial \rho_c}{\partial t} = S_c = k_c \rho_w + k_{c2}\rho_t. \quad (3)$$

The domain's initial solid mass conservation state is $\rho_{w,0}$ = 700 kg/m^3, and $\rho_{c,0}$ = 0.

The mass conservation equation for a gaseous species *i* (gas or tar) in the pyrolysis process includes diffusion, convection, and source terms,

$$\varepsilon \rho_f \frac{\partial \omega_i}{\partial t} + \nabla \cdot \mathbf{J_i} + \rho_f (\mathbf{u} \cdot \nabla)\omega_i = R_i, \quad (4)$$

where $\mathbf{J}_i$ is the diffusion flux described by Flick's law:

$$\mathbf{J_i} = -\rho_f \left(\varepsilon^{\frac{4}{3}} D_i \nabla \omega_i - \omega_i \sum_k D_k \nabla \omega_k \right). \quad (5)$$

Here ρ_f [kg/m^3] is the density of the fluid, ω_i is the mass fraction, and D_k [m^2/s] are diffusivities.

The porosity of the porous domain is

$$\varepsilon = 1 - \varepsilon_0 \frac{\rho_w + \rho_c}{\rho_{w,0}}, \quad (6)$$

ε_0 = 0.4 is the initial porosity.

Darcy's law gives the average velocity of gas:

$$\mathbf{u} = -\frac{\kappa}{\mu} \nabla P. \quad (7)$$

Here κ [m^2] is the permeability, and μ [kg/(m·s)] is the dynamic viscosity. The ideal gases equation of state provides for pressure *P*:

$$P = \frac{\rho_f R T}{\left(\sum_k \frac{\omega_k}{M_k} \right)^{-1}}, \quad (8)$$

where *M* [kg/mol] is the molecular weight and R = 8.314 [J/(mol·K] is the universal gas constant.

The source terms of gaseous species tar (*t*) and gas (*g*) are:

$$R_t = \rho \frac{\partial \omega_t}{\partial t} = k_t \rho_w - (k_{c2} + k_{g2})\rho \omega_t, \quad (9)$$

$$R_g = \rho \frac{\partial \omega_g}{\partial t} = k_g \rho_w + k_{g2} \rho \omega_t. \quad (10)$$

Mass transfer across the carbonization device's outer boundary is dominated by convection. As shown in Fig. 3, no diffusive flux exists: $\mathbf{n} \cdot \mathbf{J_i} = 0$

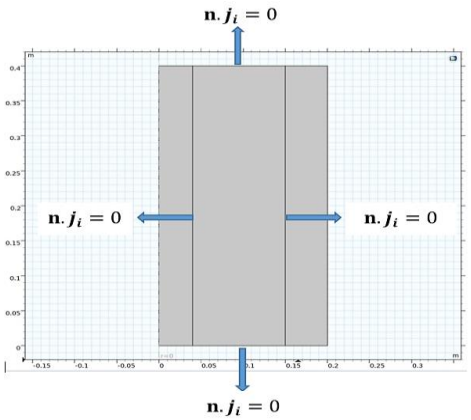

Fig. 3 – Boundary condition for gaseous species mass transport.

3.2.2. *Momentum transport*

Fluid flow in the chamber is described by the continuity equation combined with Darcy's law (eq. 7)

$$\frac{d\rho_f}{dt} + \nabla \cdot (\rho_f \mathbf{u}) = Q_m. \quad (11)$$

The mass source term Q_m [kg/m^3·s] is described by:

$$Q_m = k_t \rho_w + k_g \rho_w - k_{c2} \rho_f \omega_t. \quad (12)$$

At the outer boundary, a zero relative pressure compared to the reference pressure (P = 1 atm) is prescribed: P = 0.

3.2.3. *Energy equation*

We assume local thermal equilibrium and consider heat transfer mechanisms by convection, radiation, and conduction to model the energy balance in a porous wood sample,

$$(\rho C_P)_{\text{eff}} \frac{\partial T}{\partial t} + \nabla \cdot (-k_{\text{eff}} \nabla T) + \rho_f C_{p,f} (\mathbf{u} \cdot \nabla) T = \dot{Q}, \quad (13)$$

$$(\rho C_P)_{\text{eff}} = \varepsilon \rho_f C_{p,f} + \rho_b \left(\frac{C_{p,w} \rho_w + C_{p,c} \rho_c}{\rho_{w,0}} \right). \quad (14)$$

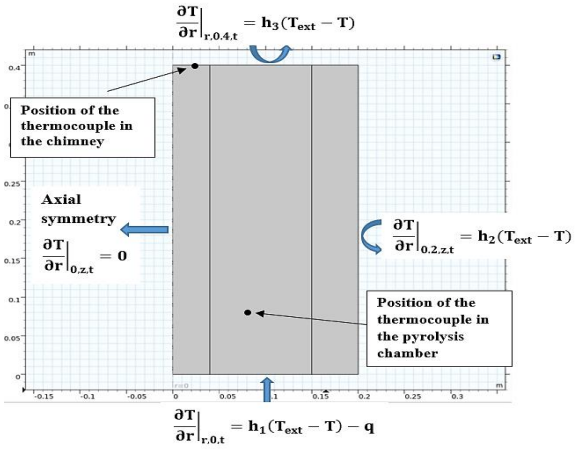

Fig. 4 – Boundary conditions of heat transfer and thermocouple positions (**q** is the autothermal influx).

The constant-pressure heat capacities for the gas and solid phases are respectively:

$$C_{p,f} = \omega_t C_{p,t} + \omega_g C_{p,g}, \quad (15)$$

The heat source term mentioned in eq. (13):

$$\dot{Q} = -\left(k_t \Delta h_t + k_g \Delta h_g + k_c \Delta h_c\right)\rho_w - (k_{g2} \Delta h_{g2} + k_{c2} \Delta h_{c2})\rho_f \omega_t. \quad (16)$$

The effective thermal conductivity depends on the fluid and solid thermal conductivities, the absolute temperature.

$$k_{\text{eff}} = \varepsilon k_f + \left(\frac{k_w \rho_w + k_c \rho_c}{\rho_{w,0}}\right) + \frac{13.5\sigma T^3 d}{e}. \quad (17)$$

where k_f = 0.0258 W/(m·K) is the thermal conductivity of the fluid, σ = 5.67·10^{-8} W/(m^2·K) is the Boltzmann constant, d = 5·10^{-5} m is the effective diameter of the pore, and ε = 0.95 is the emissivity. Boundary conditions and positions of thermocouple K are shown in Fig. 4.

3.2.4. *Momentum transport and heat transfer in the chimney*

The airflow in the chimney due to the thermosiphon effect was described using a laminar flow regime. This regime choice is based on an approximate calculation of the Reynolds number (Re ≈ 1763) and Raleigh number (Ra ≈ 4.26·10^7) [7],

$$\rho_{air}\left(\frac{\partial \mathbf{u_c}}{\partial t} + (\mathbf{u_c} \cdot \nabla)\mathbf{u_c}\right) = -\nabla p + \mu_{air}\nabla^2 \mathbf{u_c} + \mathbf{f}. \quad (18)$$

The body force term **f** includes gravity and buoyancy force given by the Boussinesq approximation [8],

$$\mathbf{f} = \rho_{air}\left(1 - \beta_{air}(T - T_{\text{ref}})\right)\mathbf{g}, \quad (19)$$

ρ_{air} is the density of the air; μ_{air} his viscosity, β_{air} the thermal expansion coefficient (1/K), g = 9.81 m/s^2 the gravity, and $T_{\text{ref}} = 298.15$ K the reference temperature. The pressure is assumed to be atmospheric at the chimney inlet and outlet. The heat equation for the chimney includes terms for accumulation, convection, and conduction. The temperature at the chimney entrance is assumed to equal the ambient. Table 2 lists specific parameter values used in the simulation.

Table 2

Materials properties and kinetics parameters.

Property	Value	Source
D_i	10^{-5} m^2/s	[21]
$C_{p,w}$	1500+1.0 x T J/(kg·K)	[9]
$C_{p,c}$	420+ 2.09 x T+6.85·10^{-5} x T^2 J/(kg · K)	[9]
$C_{p,t}$	-100+4.4 x T-1.57·10^{-3} x T^2 J/(kg · K)	[9]
$C_{p,g}$	770+0.629 x T-1.91·10^{-4} x T^2 J/(kg · K)	[9]
k_w	0.209 W/(m · K)	[5]
k_c	0.071 W/(m · K)	[5]
κ	5·10^{-16} m^2	[9]
h_1	21.95 W/(m^2 · K)	Estimated
h_2	2.58 W/(m^2 · K)	Estimated
h_3	10.76 W/(m^2 · K)	Estimated
μ	3·10^{-5} kg/(m · s)	[9]
M_g	0.038 kg/mol	[9]
M_t	0.11 kg/mol	[9]
R	8.314 J/(mol · K)	
q	2.8*10^4/t (W · s)/m^3 if t < 4800 s and 2.8*10^4 W/m^3 if t >= 4800 s	Estimated

3.3. SOLUTION STRATEGY

To solve the pyrolysis process in the carbonization device equipped with a chimney and insulated by a clay layer, the mathematical model presented above was solved numerically by the FEM implemented by [21].

- For the carbonization chamber: Darcy's law, transport of concentrated species in porous media.
- For the chimney: laminar flow and heat transfer in fluids.
- Heat transfer in solids for the clay layer.

All these physical models were solved with a time-dependent solver over 7200 s, with a time step of 1 s.

4. NUMERICAL MODELING OF THERMOELECTRIC GENERATOR

4.1. EQUATION GOUVERNING THERMOELECTRIC MODULE

A thermoelectric module consists of several elements connected and covered by ceramic plates. Each component has two types of semiconductors (p and n) connected by copper [10]. Modules are connected with heat sinks to form the thermoelectric generator [11]. The equations governing a single thermocouple are [12]:

$$-\nabla V = \rho \mathbf{J} + \alpha \nabla T, \quad (20)$$

$$\mathbf{q} = \mathrm{V}\mathbf{J} - k\nabla T + \alpha \mathrm{T}\mathbf{J}, \quad (21)$$

$$\mathbf{J} = -\sigma \nabla V - \alpha \nabla T. \quad (22)$$

Here V is the electric potential, ρ is the electric resistivity, **J** is the electric current density, α is the Seebeck coefficient, T is the temperature, **q** is the energy density flux, k is the thermal conductivity, σ is the electrical conductivity.

4.2. MODEL BUILDING AND SIMULATION

The module used for heat recovery to produce electricity, measuring 40 cm x 40 cm x 3.2 cm, comprises 127 thermocouples. Figure 5 shows the dimensions of a thermocouple. Figure 6 shows the thermal and electrical boundary conditions.

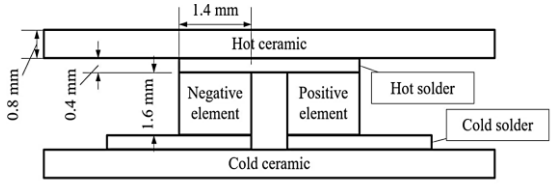

Fig. 5 – Dimensions of a thermocouple.

The materials used for the thermoelectric module simulation are selected from [21]. Alumina is assigned to the ceramic plates, copper to the semiconductor connectors, and bismuth telluride to the semiconductors.

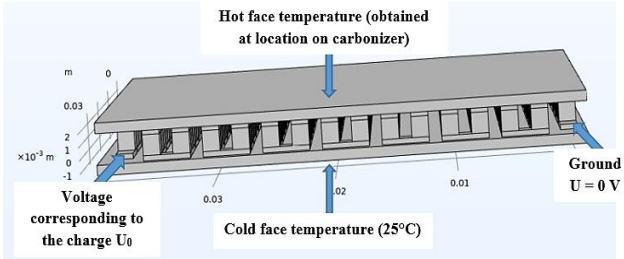

Fig. 6 – Thermal and electrical boundary conditions of the thermoelectric generator.

The steady-state regime was used to simulate the thermoelectric generator. The load voltage U_0 was varied from 0 V to 3 V for each hot side temperature in 0.5 V steps. The output current, measured with a probe, enabled the calculation of electric power P_{el},

$$P_{el} = U_0 I. \quad (23)$$

Another probe on the hot side measures the heat entering the module. The efficiency is determined by the ratio of output power to incoming thermal power,

$$\eta = \frac{P_{el}}{\dot{Q}_c}. \quad (24)$$

5. **RESULTS AND DISCUSSION**

5.1. THERMAL PROFILE OF PYROLYSIS CHAMBER

The comparison between experimentally obtained and simulated carbonization curves in Fig. 7 shows a good match. Both curves exhibit a rapid temperature rise, a plateau, and a gradual decline. After igniting the wood chips, the temperature quickly climbs to around 375 °C in the first 40 min., then rises more slowly to a maximum of 465 °C. This increase is due to the emission of combustion gases like H_2, CH_4, CO, CO_2, and volatiles, which correlate with the progression of the combustion zone. These findings align with those obtained by Mani et al. [13].

A notable difference is observed: the experimental curve fluctuates significantly, while the simulated curve is smoother. This may result from the simulation's assumption of constant thermophysical properties. The initial rise in the simulation is faster in the first ten minutes, likely because it doesn't account for biomass dehydration [14].

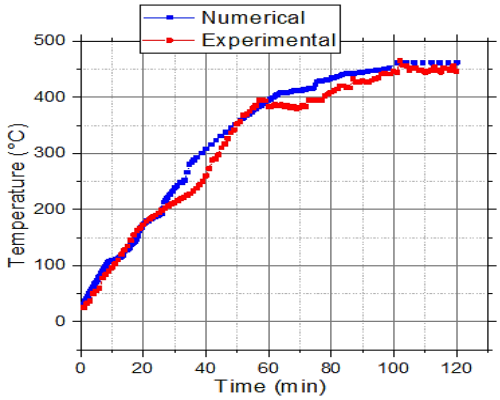

Fig. 7 – Thermal profile in the pyrolysis chamber.

The temperature in the carbonizer is influenced by several parameters, such as the increase in pressure and Darcy's velocity [15]. Figures 8 and 9 illustrate the temperature, pressure, and Darcy's velocity distribution in the carbonization chamber at two distinct moments (t = 380 s; t = 7200 s).

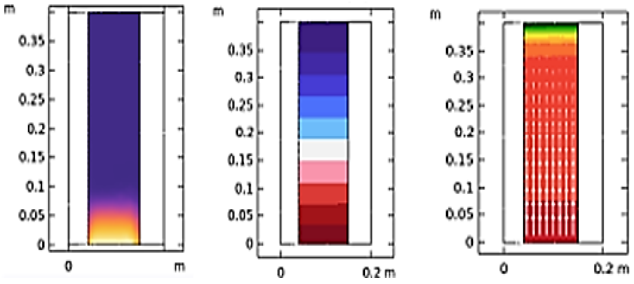

Fig. 8 – Temperature (white = 80 °C, blue = 25°C), pressure (red = $8.54{\cdot}10^6$ Pa, blue = 10^6 Pa), and Darcy's velocity (red = $4.10{\cdot}10^{-4}$ m/s, green = $1.03{\cdot}10^{-4}$ m/s) at t = 380 s.

At t = 380 s, when the thermal load is initiated at the bottom of the device, the temperature at this location is initially high, reaching a maximum of 80 °C. The pressure, influenced by the temperature, reaches a high value of $8.54{\cdot}10^6$ Pa in the affected area. The Darcy velocity ranges from $1.03{\cdot}10^{-4}$ m/s to $4.10{\cdot}10^{-4}$ m/s, with the maximum observed in the hottest area.

At the end of the carbonization process (t = 7200 s) as shown in Fig. 9, the temperature in the carbonizer is uniform at 447 °C, with a slight decrease near the walls in contact with the chimney and the clay layer.

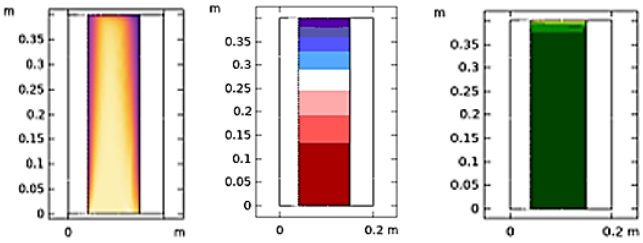

Fig. 9 – Temperature (yellow = 447 °C, blue = 127 °C), pressure (red = $17.1{\cdot}10^6$ Pa, blue = 10^5 Pa), and Darcy's velocity at t = 7200 s.

Due to the accumulation of pyrolysis gases, the pressure reaches a maximum of 17.1[illegible]106 Pa, while the Darcy velocity is nearly uniform at $0.4{\cdot}10^{-3}$ m/s.

Initially, temperature rises gradually with low pressure and minimal Darcy's velocity. As pyrolysis starts, volatile gases increase pressure and heat transfer. Combustion of these gases raises temperature further, stabilizing pressure. A thermal plateau is then reached where reactions and heat dissipation balance.

5.2. THERMAL PROFILE OF CO-GENERATED HOT AIR

The chimney in a carbonizer evacuates gases and smoke, boosts natural convection, controls temperature, ensures safety, and impacts the charcoal yield [16]. The density difference between hot and cooler air drives natural convection. This density difference creates buoyancy pressure that moves the air, as shown in Fig. 10, illustrating the airflow velocity in the chimney due to the temperature increase.

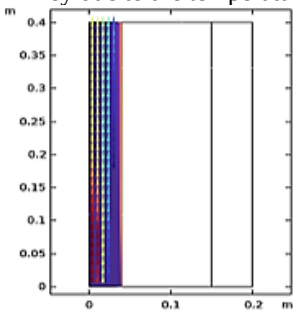

Fig. 10 – Temperature and airflow in the chimney (red arrow = 3.1 m/s, blue arrow = 2.75 m/s) at t = 7200 s.

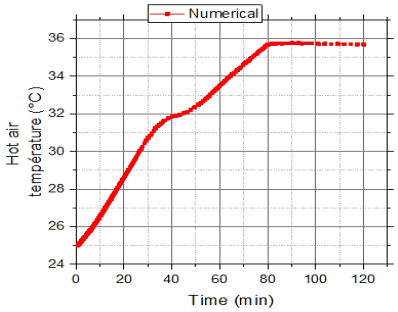

Fig. 11 – Thermal profile of co-generated hot air.

Figure 11 shows the numerical thermal profile of the hot air measured by the thermocouple placed at the chimney outlet. The chimney's temperature rises rapidly for the first 80 min before plateauing, with an 11 °C gain, lower than the 20 °C experimental

maximum. This discrepancy may be due to pyrolysis plumes escaping through small chimney holes.

Figure 12 illustrates the variation of energy flux at the chimney outlet, which increases gradually before stabilizing after approximately 80 minutes.

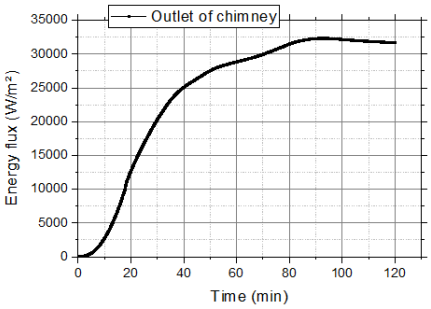

Fig. 12 – Energy flux at the outer of chimney.

Despite the low-temperature gain, a TEG module could be installed at the chimney outlet. A probe measured a maximum energy flux of 32.000 W/m² after 80 minutes. With an efficiency of approximately 4×10^{-3}, due to the low-temperature gradient, the TEG would produce 128 W/m² according to formula (24). Optimizing the system could improve hot air recovery for drying or heating. The air circulation speed varies between 2.75 m/s and 3.1 m/s, with the maximum speed observed in the hottest areas.

5.3. THERMOELECTRIC MODULE INSTALLATION SITE

Energy efficiency, module protection, and cost must be considered to optimize the placement of the thermoelectric module on a carbonizer. Studies show peak temperatures around 120 min into the process. Modules can be placed at the carbonization chamber boundary if they withstand up to 300 °C. However, operating at up to 200 °C is recommended for longevity [17]. The ideal placement range is 0.26 m to 0.3 m from the boundary, where temperatures are 25 °C to 194 °C, ensuring optimal performance and durability. Figure 13 shows the temperature variation at the carbonization chamber boundary at t = 7200 s, while Fig. 14 shows the temperature in the 0.26 m - 0.3 m section selected for module installation.

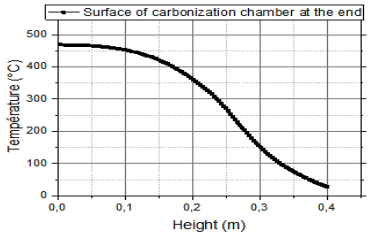

Fig. 13 – Temperature at the surface of the carbonization chamber at t = 120 min.

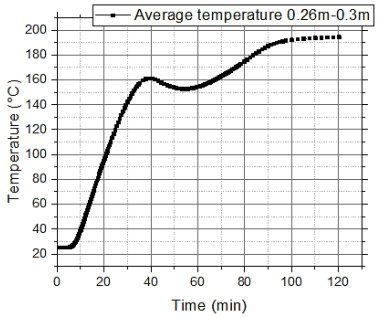

Fig. 14 – Temperature between the 0.26 m – 0.3 m portion.

The temperature initially rises due to external heating, drops slightly as pyrolysis absorbs heat, and then increases again as gases ignite or are evacuated [18]. It eventually levels off when heat from reactions balances with dissipation, indicating the end of carbonization and the formation of charcoal.

5.4. NORMALIZED SOLID MASS

The normalized solid mass is the ratio of the total solid mass at a given time to the initial solid mass. It is shown in Fig. 15. At the beginning of carbonization, the solid mass changes slowly in the first ten minutes due to the gradual temperature rise, which is insufficient for rapid decomposition. Wood's thermal inertia causes it to absorb heat and increase the internal temperature before significant decomposition starts. Following this phase, rapid mass variation occurs, likely due to the chemical composition of wood—mainly cellulose, hemicellulose, and lignin [19].

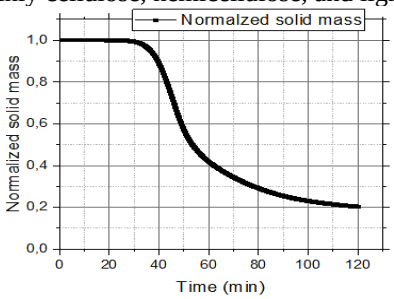

Fig. 15 – Normalized solid mass.

After 100 minutes, the mass loss stabilizes at 0.21, indicating nearly complete carbonization and stable solid residue. The experimental charcoal yield is 20.89%, closely matching the simulation result of 21%.

5.5. ELECTRICAL QUANTITIES OF THE MODULE OBTAINED FROM SIMULATION

The module's location is crucial to ensure optimal operation. The chosen position is illustrated in Fig. 16.

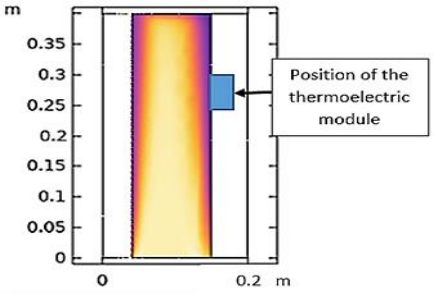

Fig. 16 – Position of thermoelectric module.

Once installed, the temperature gradient across the module generates a voltage. Figure 17 shows the temperature distribution at t = 7200 s (a) and the voltage distribution with a 3 V load applied to the module terminals (b).

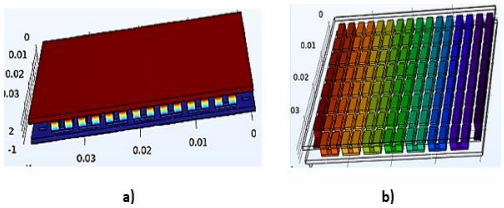

Fig. 17 – a) Temperature distribution at t = 7200 s (red = 194 °C, blue = 25°C);
b) voltage distribution for U_0 = 3 V (red = 3 V, violet = 0 V).

Figure 18 presents the voltage and power variation as a current function for a hot side temperature of the thermoelectric module *Th* = 194 °C obtained at *t* = 7200 s. These graphs allow for extracting several important electrical quantities for this temperature. In this study, the maximum power generated by the module can reach up to 6.5 W. This maximum value is obtained at the end of the carbonization process, suggesting that it is at this moment that the module produces the most electrical energy.

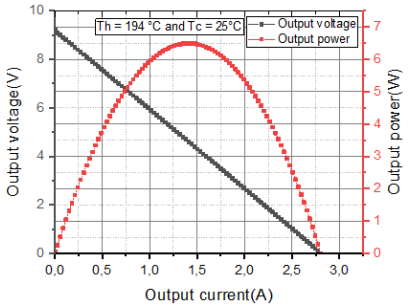

Fig. 18 – Current-voltage-power for the maximum temperature (*Th* = 194 °C).

As shown in Fig. 19, the efficiency of a thermoelectric module strongly depends on the load voltage for a given temperature gradient.

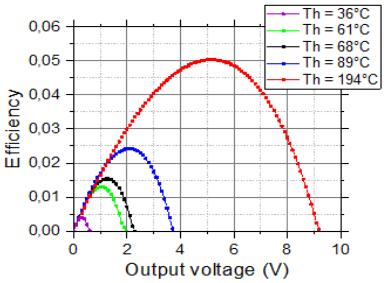

Fig. 19 – Efficiency for various hot face temperatures of the module.

5. **CONCLUSION**

This article comprehensively evaluates integrating thermoelectric modules with biomass carbonization processes, employing both experimental and numerical analyses using FEM [20]. The research identifies optimal conditions where thermoelectric modules can operate efficiently by carefully analyzing thermal profiles and module placement.

The module, positioned strategically, can recover up to 6.5 W of electricity from the heat generated during carbonization.

The findings emphasize the dual benefits of this integration: it enhances the energy efficiency of the carbonization process and provides a renewable energy source through electricity generation. The integration of the chimney increased the air temperature by 11 °C above ambient temperature.

Future optimization could achieve even higher temperatures, which would be helpful for drying and heating.

ACKNOWLEDGMENTS

The first author expresses his deep gratitude for the financial support of the Agence Universitaire de la Francophonie (AUF), which made this research possible. We also thank the Laboratory of Conversion and Energy Sources and the Multiphysics Modeling Laboratory of the Faculty of Electrical Engineering at the National University of Sciences and Technologies Politehnica of Bucharest for their valuable collaboration and indispensable technical resources.

Received on 11 August 2024

Credit authorship contribution statement. Hervé Klinklin Badaka: Writing, experimental work, numerical simulation. Alexandru M. Morega: Physical-mathematical overview, numerical simulation data analysis.

REFERENCES

1. A.M. Omer, *Sustainable development and environmentally friendly energy systems in Sudan*, Adv. Environ. Res., **36**, *1*, pp. 51–94 (2014).
2. Y. Zhang, Y. Ji, H. Qian, *Progress in thermodynamic simulation and system optimization of pyrolysis and gasification of biomass*, Green Chem. Eng., **2**, *3*, pp. 266–283 (2021).
3. D. Champier, J. Bédécarrats, T. Kousksou, M. Rivaletto, F. Strub, P. Pignolet, *Study of a TE (thermoelectric) generator incorporated in a multifunction wood stove*, Energy, **36**, *3*, pp. 1518–1526 (2011).
4. A. Radenović, *Pyrolysis of coal*, Kem. u Ind. Chem. Eng., **55**, *7*, pp. 311–319 (2006).
5. W.C. Park, A. Atreya, H.R. Baum, *Experimental and theoretical investigation of heat and mass transfer processes during wood pyrolysis*, Combust. Flame, **157**, *3*, pp. 481–494 (2010).
6. A. Kulkarni, G. Mishra, S. Palla, P. Ramesh, D. Surya, T. Basak, *Advances in computational fluid dynamics modeling for biomass pyrolysis: a review*, Energies, **16**, *23*, pp. 1–32 (2023).
7. J.P. Abraham, E.M. Sparrow, J.C.K. Tong, *Heat transfer in all pipe flow regimes: laminar, transitional/intermittent, and turbulent*, Int. J. Heat Mass Transf., **52**, *3*, pp. 557–563, (2009).
8. D.D. Gray, A. Giorgini, *The validity of the Boussinesq approximation for liquids and gases*, Int. J. Heat Mass Transf., **19**, *5*, pp. 545–551 (1976).
9. M.G. Gronli, M.C. Melaaen, *Mathematical model for wood pyrolysis-comparison of experimental measurements with model predictions*, Energy and Fuels, **14**, *4*, pp. 791–800 (2000).
10. B. Geppert, D. Groeneveld, V. Loboda, A. Korotkov, A. Feldhoff, *Finite-elements simulations of a thermoelectric generator and their experimental validation*, Energy Harvest. Syst., **2**, *1*, pp. 95–104 (2015).
11. Y. Köysal, *Performance analysis on solar concentrating thermoelectric generator coupled with heat sink*, Int. J. Precis. Eng. Manuf., **20**, *2*, pp. 313–318 (2019).
12. A. Morega, M. Morega, *A FEM model of thermoelectric and thermomagnetic effects*, Rev. Roum. Sci. Techn. – Électrotechn. et Énerg., **48**, *1*, pp. 2 (2003).
13. D. Mani, P. Kpelou, N. Attah, S. Kombate, *Energy resource of charcoals derived from some tropical fruits nuts shells*, Int. Journal of Renewable Energy Development, **9**, *1*, pp. 29–35 (2020).
14. A. Demirbas, *Effect of initial moisture content on the yields of oily products from pyrolysis of biomass*, J. Anal. Appl. Pyrolysis, **71**, *1*, pp. 803–815 (2004).
15. G.Qi, Z. Wang, S. Zhang, Y. Dong, J. Guan, P. Dong, *Numerical simulation on biomass-pyrolysis and thermal cracking of condensable volatile component*, Int. J. Hydrogen Energy, **45**, *22*, pp. 12283–12297 (2020).
16. J. Prapas, M. Baumgardner, A. Marchese, B. Willson M. DeFoort, *Influence of chimneys on combustion characteristics of buoyantly driven biomass stoves*, Energy Sustain. Dev., **23**, *1*, pp. 286–293 (2014).
17. R. Hall, *An analysis of the performance of thermoelectric devices made from long-lifetime semiconductors*, Solid State Electron., **2**, *3*, pp. 115–122 (1961).
18. H.C. Kung, *A mathematical model of wood pyrolysis*, Combust. Flame, **18**, *2*, pp. 185–195 (1972).
19. F.X. Collard, J. Blin, *A review on pyrolysis of biomass constituents: Mechanisms and composition of the products obtained from the conversion of cellulose, hemicelluloses, and lignin*, Renew. Sustain. Energy Rev., **38**, *1*, pp. 594–608 (2014).
20. K. Sornek, M. Filipowicz, *A study of the applicability of a straw-fired batch boiler as a heat source for a small-scale cogeneration unit*, Chemical and Process Engineering., **37**, *4*, pp. 503–515 (2016).
21 *Comsol Multiphisics*, v.6.2.